Front. Earth Sci. 2021, 15(4): 860–875
https://doi.org/10.1007/s11707-021-0919-4

RESEARCH ARTICLE

Pore structure complexity and its significance to the petrophysical properties of coal measure gas reservoirs in Qinshui Basin, China

Xiaowei HOU[1], Yang WANG (✉)[2,3], Yanming ZHU[2,3], Jie XIANG[2,3]

1 School of Resources and Environmental Engineering, Hefei University of Technology, Hefei 230009, China
2 Coalbed Methane Resources and Reservoir Formation Process Key Laboratory of Ministry of Education, China University of Mining & Technology, Xuzhou 221008, China
3 School of Resources and Geoscience, China University of Mining & Technology, Xuzhou 221116, China

Abstract The pore structure of continuous unconventional reservoirs (CURs) in coal measures was investigated using different technologies for 29 samples (9 coal samples, 9 shale samples, and 11 sandstone samples) from Qinshui Basin, China. Results show that coals have relatively high porosities and permeabilities ranging from 4.02% to 5.19% and 0.001 to 0.042 mD, respectively. Micropores (<2 nm) are well-developed in coals and contribute to the majority of pore volume (PV) and specific surface area (SSA). The porosities and permeabilities are between 1.19%–4.11%, and 0.0001–0.004 mD of sandstones with a predominance of macropores (>50 nm). However, shales are characterized by poorly petrophysical properties with low porosity and permeability. Macropores and mesopores (2–50 nm) are well-developed in shales compared with micropores. For coals, abundant organic matters are expected to promote the development of micropores, and clay minerals significantly control the performance of mesopores. For shales and sandstones, micropores are mainly observed in organic matters, whereas clay minerals are the important contributor to mesopores. Moreover, micropore SSA significantly determines the adsorption capacity of CURs and sandstones have the best pore connectivity. The permeability of CURs is positively associated with the macropore PV since macropores serve as the main flow paths for gas seepage. Additionally, we also proposed that effective porosity has a significant effect on the permeability of CURs. The findings of this study could enhance the understanding of the multiscale pore structure of CURs and provide insights into the mechanisms that control gas storage, transport, and subsequent co-production for continuous unconventional natural gas (CUNG) in the Qinshui Basin and other coal-bearing basins worldwide.

Keywords continuous unconventional reservoirs (CURs), pore structure, adsorption capacity, permeability, effective porosity

1 Introduction

The worldwide boom in unconventional gas has become increasingly important in the balance of natural gas production. Previous studies have reported that coalbed methane (CBM), shale gas, and tight sandstone gas (TSG) can be developed continuously in adjacent strata in the same coal-bearing basin and a combination of these gases were also named continuous unconventional natural gas (CUNG) in coal measures (Li et al., 2016, 2019a; Hou et al., 2017). Different from an independent natural gas, gas within different CURs migrate via a short flow path nearby reservoirs and interact with others (Ayers, 2002; Law and Curtis, 2002; Wang et al., 2014; Schmitt et al., 2015; Wang et al., 2016; Monaghan, 2017; Ghomeshi et al., 2018). With the advanced technology and increasing demand for energy resources, the co-production of CUNG has expanded rapidly around the world and some pioneering efforts have been tried in the Ordos and Qinshui basins (Li et al., 2017, 2019b; Hou et al., 2018). The heterogeneous and complex pore structure is the primary flow path for CUNG storage and transport (Ross and Bustin, 2008; Loucks et al., 2009; Mishra et al., 2018). Moreover, it is believed that pore structure significantly affects petrophysical properties for a reservoir play, such as

Received February 2, 2021; accepted June 10, 2021

E-mails: hxw15162167321@163.com (Xiaowei HOU)
wangycumt@163.com (Yang WANG)

sorption behavior and permeability (Krooss et al., 2002; Ross and Bustin, 2008; Yao and Liu, 2012; Zhang et al., 2016; Huang et al., 2018). Based on the pore size classification proposed by IUPAC (1994), pores can be classified into three types: micropores (< 2 nm), mesopores (2–50 nm), and macropores (> 50 nm), respectively. The pore structure of unconventional reservoirs has been comprehensively studied using various methods, including capture technologies such as optical microscopy and field emission scanning electron microscopy (FE-SEM) and fluid intrusion methods such as high-pressure mercury intrusion porosimetry (HPMI), low-pressure gas (N_2/CO_2) adsorption (N_2GA, CO_2GA). Image capture technologies are suitable for qualitatively describing pore morphology features at nano- to micron-scales, whereas these measurements cannot give a quantitative evaluation for nanopores (Bernard et al., 2012; Nie et al., 2015; Mishra et al., 2018). Fluid intrusion methods have been widely used to quantitatively obtain pore structure parameters, such as pore size distribution (PSD), specific surface area (SSA), and pore volume (PV) (Wang et al., 2014: Nie et al., 2015; Zhao et al., 2016; Sun et al., 2017), but N_2GA and CO_2GA fail to determine the pore structures of macropores with large size (Wang et al., 2014; Hou et al., 2020c; Li et al., 2020; Song et al., 2020; Wang et al., 2020; Yang and Liu, 2020). Theoretically, the NMR method has been proven to be a non-destructive and quantitative method capable to determine pores on a wide scale. Therefore, the NMR method has been popularly applied to evaluate the pore structure for porous media (Yao and Liu, 2012; Li et al., 2018).

The multiscale pore system within CURs is the internal factor directly influencing the storage and transport behaviors of CUNG. However, full-scale determination of the pore structure and comparative analysis among various CURs is still a challenging work. Therefore, a combination of different experimental technologies is necessary for a systematic illustration of the full-scale pore structure of CURs. In this study, the pore structure and its significance to the petrophysical properties of CURs in Qinshui Basin were studied using a combination of various experimental technologies, including optical microscopy, FE-SEM, HMIP, N_2GA, CO_2GA, and NMR.

2 Materials and methods

2.1 Geological background and samples

The Qinshui Basin is an important petroliferous, intracratonic basin in China where contains abundant CUNG resources. Co-production of CUNG resources with good potential has been proven in the Yushe-Wuxiang area located at the central east Qinshui Basin (Hou et al., 2017). The tectonic evolution of the study area experienced four primary stages: 1) The rapid subsidence stage occurred in the late Hercynian to Indosinian orogenesis. Approximately 3000–4000 m of the overlying strata were deposited on top of the target coal-bearing strata; 2) During the early Yanshanian orogeny, the burial depth of the coal-bearing strata was slightly undulatory and suffered compression under the NW-SN toward tectonic stress due to alternating subsidence and uplift of the lithosphere; 3) During the period of middle and late Yanshanian orogenesis, the area was compressed again causing a significant uplift of the coal-bearing strata; and 4) During the Himalayan orogeny, the NNW-SSE directional tension stress made the coal-bearing strata rapidly uplift (Hou et al., 2020a). To avoid interference from the effect of tectonism on the pore structure of CURs, 9 shale samples, 11 sandstone samples, and 9 coal samples under the same tectonic evolution were collected from the drilling well, and the surrounding coal mines in the Yushe-Wuxiang area, Qinshui Basin. Shale and sandstone samples were collected from the same well (well zk7-1), and coal samples were collected from the main coal seams of three coal mines, as shown in Fig. 1. The vitrinite reflectance (R_o) values of coal and shale samples range from 2.15% to 2.90%, suggesting the coalification of the source rocks in the study area mainly entered the overmature level.

2.2 Experimental methods and procedures

All of the samples were drilled into core plugs (2.5 cm in diameter and 4–5 cm in length) for NMR and pressure pulse decay permeability/porosity measurements. Moreover, the residual cuttings of the samples were used for optical microscopy, FE-SEM, HPMI, N_2GA, CO_2GA, total organic compound (TOC), X-ray diffraction (XRD), and vitrinite reflectance (R_o) measurements.

The organic-inorganic components and relevant contents of the selected samples were detected by TOC and XRD analyses using a Leco CS-230 analyzer and a RIGAKU D/Max-3B diffractometer, respectively, at the Experimental Research Center of East China Branch, SINOPEC. R_o value was measured using a DM4500P polarizing microscope at the Key Laboratory of Coalbed Methane Resources and Reservoir Formation Process (Ministry of Education), China University of Mining and Technology. Moreover, pore morphologies of CURs were observed using a petrographic microscope and a Quanta 200 F equipped with an energy-dispersive spectrometer (EDS) on surfaces prepared by Arion milling at the Jiangsu Design Institute of Geology for Mineral Resources.

HPMI experiments were conducted on an Auto Pore IV 9500 at the Key Laboratory of Coalbed Methane Resources and Reservoir Formation Process (Ministry of Education), China University of Mining and Technology to determine the pore structure of pores with the scale of 3 nm to 100 mm. Before the experiment, the samples were processed into bulks of about 1 cm^3 and dried for 12 h at

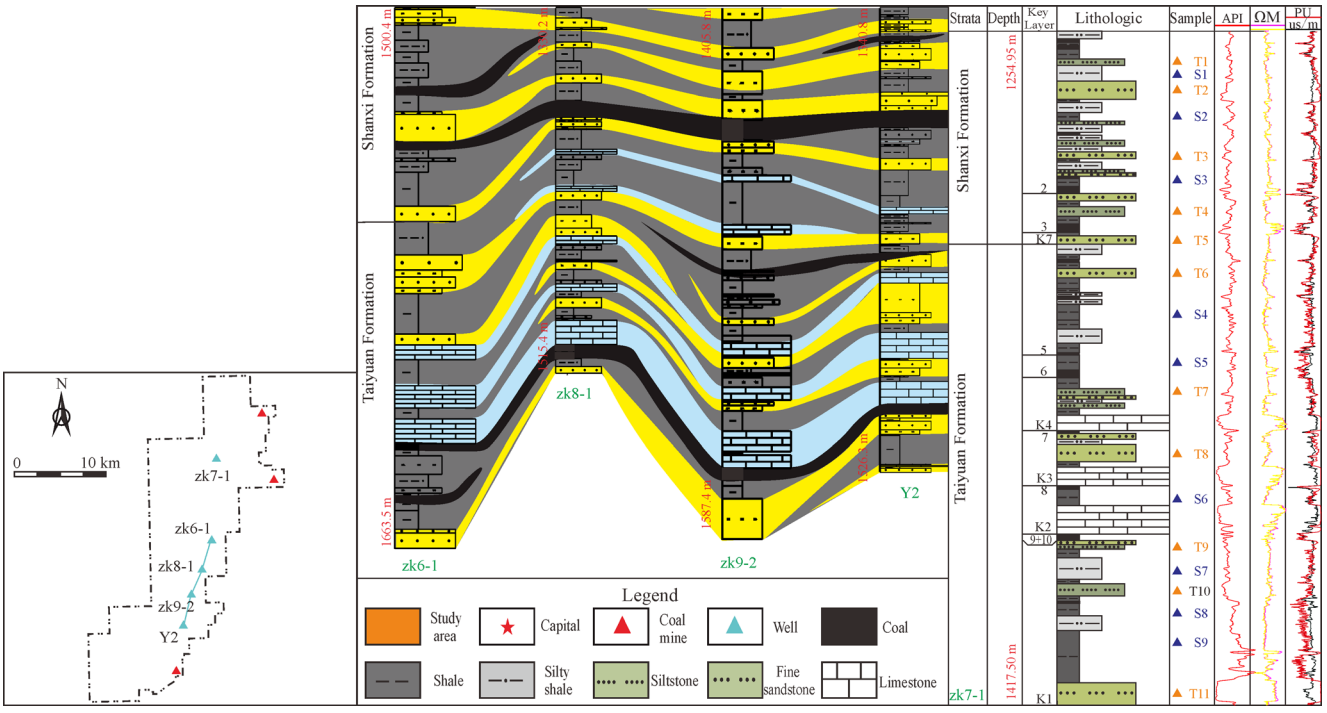

Fig. 1 Sampling locations and geological setting of the Yushe-Wuxiang area, Qinshui Basin.

70°C–80°C. During the experiment, the pressure was increased from 0.01 to 413 MPa in the mercury intrusion phase and then gradually decreased in the mercury ejection phase.

The N_2GA and CO_2GA analyses were performed at a Quantachrome Autosorb-1 at the Key Laboratory of Coalbed Methane Resources and Reservoir Formation Process (Ministry of Education), China University of Mining and Technology to determine pore structure characteristics of PV, SSA, and PSD for the tested samples. The employed samples were crushed into 40–60 mesh and dried for 8 h at 70°C to remove the moisture and other volatiles and then they were performed at different gas adsorption levels in nitrogen and CO_2 atmospheres, respectively.

Moreover, the NMR tests were performed on saturated and centrifuged plug samples to obtain the T_2 spectrums using a MesoMR23-060H-I at the Experimental Research Center of East China Branch, SINOPEC. Pressure pulse decay permeability/porosity tests were conducted using a CoreLab/Temco PDP-200 with an accuracy of 0.00001 mD to obtain permeability and porosity for a given confining pressure at the Key Laboratory of Coalbed Methane Resources and Reservoir Formation Process (Ministry of Education), China University of Mining and Technology. The employed samples were first processed into lithologic columns of diameter of 2.5 cm and length of 5.0 cm, with the top and bottom surfaces polished to obtain parallel ends. The permeability of the samples was determined under a constant inlet pressure.

3 Results

3.1 Mineralogical components and physical properties of CURs

The coals mainly consisted of aggregate organic matters with high TOC ranging from 76.45% to 90.10% (avg. 86.39%) and macerals showed a clustered distribution, as shown in Figs. 2(a) and 2(b). Inorganic minerals in the coals were dominated by clay minerals embedded in organic macerals (Figs. 2(i) and 2(j)). For shales, the organic matters displayed a dispersed or granular distribution and TOC contents were between 1.25% and 3.25% (avg. 2.27%). Clay and quartz minerals were mainly inorganic components of shales, and their contents varied from 39.7% to 54.9% (avg. 46.6%), and 36.4% to 56.9% (avg. 42.9%), respectively. However, a favorable amount of organic matter was also found in the sandstone samples with a range of 0%–4.56% since sandstone layers in coal-bearing strata were interbedded in coals and shales. During deposition, organic matters in coals or shales experienced river channel erosion, resulting mixture of organic grains and strips with sandstones (Hou et al., 2020c). Inorganic components of sandstones were dominated by quartz, which ranged from 37.6% to 78.0% (avg. 52.2%). Clay, feldspar, and carbonate minerals comprised the minor proportions of the inorganic component in sandstones.

For coals, abundant organic pores were found in the organic macerals (Figs. 2(a), 2(b), 2(i), and 2(j)). These pores included cell pores (Fig. 2(a)) and blowholes

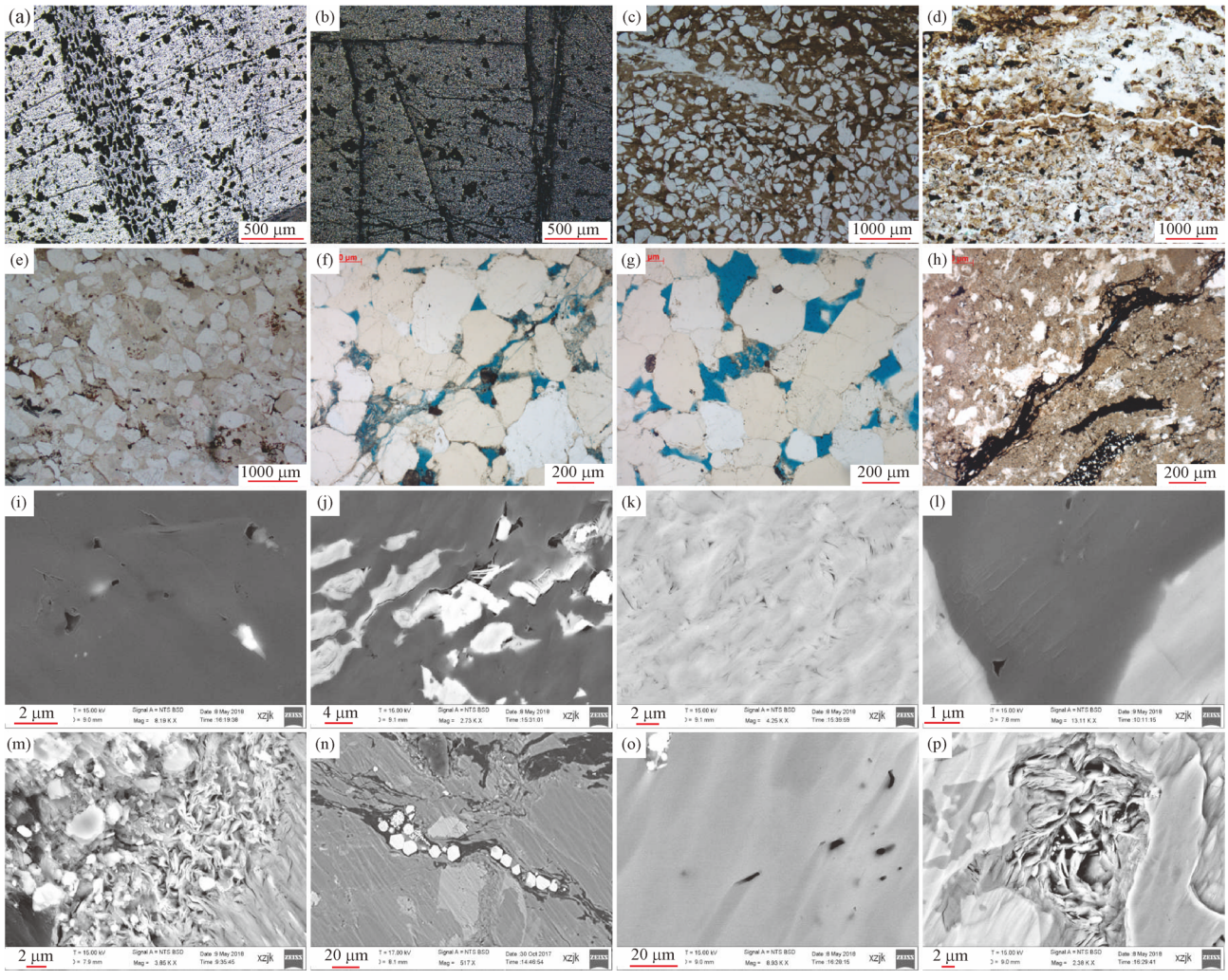

Fig. 2 Photomicrographs showing the pore systems of the CURs. (a) Cell pores, dispersed organic pores, and microfractures of coal sample C3; (b) blowholes and microfractures in vitrinite, C1; (c) intergranular pores and dispersed organic matter of shale sample S2; (d) dispersed organic matter and microfractures filled by calcspar of shale sample S4; (e) intergranular pores of shale sample S2; (f) dispersed organic matter, intergranular pores developed along the edges of rigid quartz grains and interfaces between quartz grains and clay minerals of sandstone sample T8; (g) intergranular pores and dissolved pores of sandstone sample T6; (h) banded organic matter in sandstone sample; (i) isolated organic pores (blowholes) of coal sample C2; (j) primary pores filled by clay mineral, intergranular pores between organic macerals and clay minerals, and aggregated intragranular pores in clay minerals of coal sample C4; (k) aggregated intragranular pores in clay minerals of coal sample C6; (l) organic pores of shale sample C6; (m) intragranular pores in clay minerals, and intergranular pores between organic macerals and clay minerals of shale sample C4; (n) organic band filled by pyrite grains with abundant intergranular pores, organic pores and intergranular pores of sandstone sample T10; (o) dissolved pores in feldspar of sandstone sample T5; and (p) intergranular pores and intragranular pores in clay minerals of sandstone sample T9.

(Figs. 2(b) and 2(i)), where a part of the primary pores was significantly filled by clay minerals (Fig. 2(j)), resulting in beaded and banded intergranular pores at the interfaces between macerals and clay minerals. Moreover, aggregated intragranular pores were well developed in clay minerals (Figs. 2(j) and 2(k)), and some microfractures were also observed in macerals. For shales, the pore framework consisted of inorganic minerals including clay minerals and rigid quartz grains (Wang et al., 2014). Abundant aggregated intragranular pores were developed in clay minerals and intergranular pores and microfractures were found between quartz grains (Fig. 2(m)). Moreover, dispersed organic pores were observed in organic matter (Figs. 2(c), 2(d), and 2(l)). Additionally, the pore framework of sandstones was mainly provided by rigid quartz grains (Lai et al., 2018). Therefore, intergranular pores and microfractures were well developed along the edges of rigid quartz grains (Figs. 2(f) and 2(g)) (Lai et al., 2018). In addition, abundant aggregated intragranular pores (Fig. 2(p)) and dispersive dissolved pores (Fig. 2(o)) were also observed in clay minerals and unstable minerals, such as feldspar, respectively.

Generally, CURs are characterized by low porosity and permeability (porosity $< 10\%$, permeability $< 10^{-3}$ μm^2).

The ranges of porosities of coals, shales, and sandstones were 4.02%–5.19% (avg. 4.71%), 0.66%–2.65% (avg. 1.62%), and 4.02%–5.19% (avg. 4.71%), respectively. Coals had the largest permeability, which ranged from 0.001 to 0.042 mD (avg. 0.024 mD), followed by sandstones with a range of 0.0001–0.004 mD (avg. 0.001 mD), while the permeability of shales was the lowest at 0.0002–0.002 mD. Note that fractures/cleats with relatively large scale were well-developed in coal reservoirs and thus contributed to the relatively high porosity and permeability. Moreover, permeability was weakly correlated with total porosity, as shown in Fig. 3, indicating that the pore structure played a significant role in controlling the permeability of CURs (Xiao et al., 2018).

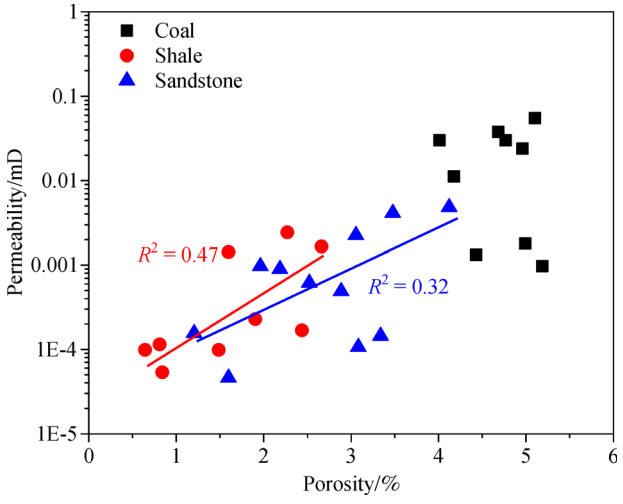

Fig. 3 Relationship between porosity and permeability.

3.2 HMIP analyses

3.2.1 Physical properties and pore types

The mercury injection and ejection curves can be subdivided into two types, corresponding to different pore morphologies (Chen et al., 2012). For coals, Type I was characterized by a rapidly increasing mercury injection volume without saturation at a pressure of more than 10000 psi, indicating micropores were well-developed. The hysteresis loop was broad, corresponding to open pores and semi-closed pores, as shown in Fig. 4(a). Type II was characterized by a significantly increasing mercury injection volume at pressures of < 10 psi and > 10000 psi with very minor hysteresis loops, indicating the dominance of semi-closed pores in the pore morphology, as shown in Fig. 4(b).

For Type I of shales, the mercury injection volume increased rapidly without any saturation at a pressure of > 10000 psi which suggested that micropores were also well-developed, as shown in Fig. 4(c). The hysteresis loops are broad, corresponding to open pores and semi-closed pores. However, a rapid increase at a pressure of < 10 psi with broad hysteresis loops was found in Type II of shales which implied that the pore morphologies were dominated by open pores combining with a number of bottleneck pores, as shown in Fig. 4(d).

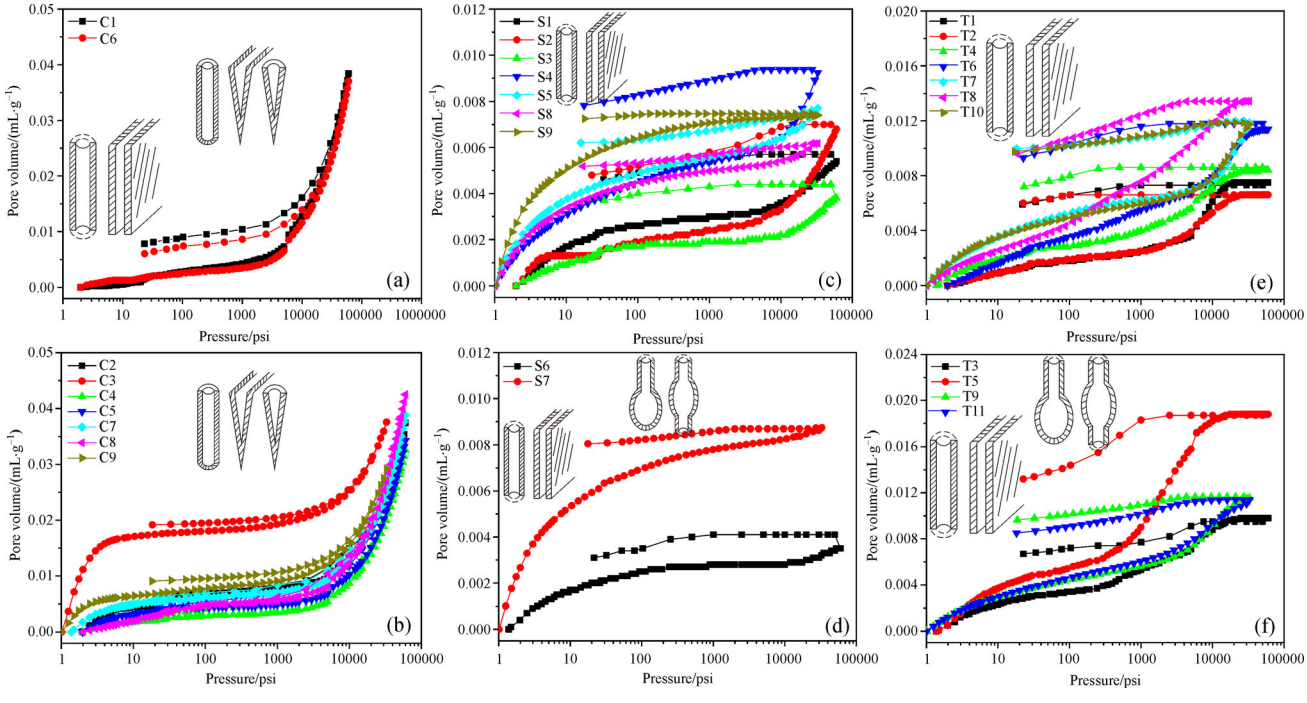

Fig. 4 Mercury injection and ejection curves of CURs: (a) and (b) coals; (c) and (d) shales; (e) and (f) sandstones.

For sandstones, Type I curves exhibited significantly increased mercury injection volume at a pressure of < 10000 psi, and saturation was reached at pressures over 10000 psi, suggesting micropores were poorly developed. The hysteresis loop was broad, corresponding to an open pore system, as shown in Fig. 4(e). The hysteresis loop of Type II was similar to that of Type I and pore morphology was also dominated by open pores with some fine bottleneck pores, as shown in Fig. 4(f). The effective pores of CURs included two main types: open pores and semi-closed pores (Song et al., 2017). From the analyses above, the development of effective pores in sandstones and shales was better than that in coals, resulting in the relatively high pore connectivity of sandstones and shales.

Pore structure parameters SSA, PV, and average diameter were also determined through HPMI analyses, as listed in Table 1. The SSAs of CURs followed the order of coal > shale > sandstone, whereas the reverse trend was observed in the average diameter of CURs (coal < shale < sandstone). The SSAs of coals, shales, and sandstones ranged from 6.47 to 23.35 m^2/g (avg. 17.19 m^2/g), 0.07 to 2.55 m^2/g (avg. 0.93 m^2/g), and 0.72 to 2.09 m^2/g (avg. 1.22 m^2/g), respectively. The average diameters of coals, shales, and sandstones ranged from 7.2 to 23.2 nm (avg. 10.6 nm), 10.6 to 61.8 nm (avg. 27.9 nm), and 22.7 to 80.5 nm (avg. 40.4 nm), respectively. The coals had the highest PV at 0.0066–0.0134 mL/g (avg. 0.0113 mL/g), followed by sandstones.

3.2.2 Characterization of PSDs

The PSDs of CURs can be also classified into two types. For coals, Type I was characterized by a unimodal distribution with a dominant peak of < 100 nm, as shown in Fig. 5(a). In contrast, Type II showed a bimodal distribution with peaks within the size scales of < 100 nm and > 100000 nm, as shown in Fig. 5(b). Note that the main peak was mainly located at zones of pore sizes < 100 nm. For shales, Type I (Fig. 5(c)) and Type II (Fig. 5(d)) were characterized by the unimodal distribution and bimodal distribution, respectively. The peaks of Type II were at the size ranges of < 100 nm and > 100000 nm, and the main peak was dominated by the pore size of > 10000 nm. For sandstones, Type I had a bimodal PSD with a major peak of < 100 nm (Fig. 5(e)), but Type II had a multimodal distribution, as shown in Fig. 5(f).

3.3 N_2GA results

3.3.1 Physical properties and pore types

The results of N_2GA adsorption and desorption curves were shown in Fig. 6. The N_2GA sorption isotherms of the samples were of Type IV according to the IUPAC classification with a sharp uptake in the saturated vapor pressure. Based on the shapes of the hysteresis loops, two types can be identified for the tested samples (Song et al., 2017). For coals, Type I hysteresis loop was very narrow and can be classified as type H3 recommended by IUPAC (Fig. 6(a)), indicating that the pore morphologies were slit-shaped with one side almost closed and tubular with two sides open. Type II hysteresis loops were characterized by small loops, representing H3 and H4 curves recommended by the IUPAC (Fig. 6(b)). These loops correspond to tubular pores and parallel plate pores with all sides open, with some fine bottleneck pores. Type I hysteresis loops of shales were similar to those of sandstones with wide loops, representing H2, which also had the features of H1 and H3 types recommended by the IUPAC (Figs. 6(c) and 6(f)). These types correspond to a complicated pore system, which mainly comprises tubular pores and parallel plate pores with all sides open. For shales and sandstones, Type II loops were characterized by small hysteresis loops, featuring the characteristics of H3 and H4 curves recommended by the IUPAC (Figs. 6(d) and 6(e)). These curves correspond to a pore morphology dominated by tubular pores and parallel plate pores with all sides open, with some fine bottleneck pores. The pore morphology of CURs obtained by N_2GA indicated that the pore connectivity of sandstones and shales was better than that of coals.

N_2GA analyses also provided results of BET SSA, DFT PV, and average pore diameter, respectively. Coals had poor PVs and SSAs, with large average pore diameters. The PVs, SSAs, and average pore diameters ranged from 0.0007 to 0.0056 mL/g (avg. 0.0016 mL/g), 0.09 to 1.36 m^2/g (avg. 0.48 m^2/g), and 6.76 to 33.76 nm (avg. 16.67 nm), respectively. Shales were characterized by large SSAs, medium PVs, and small average pore diameters which were between 2.97 and 6.00 m^2/g (avg. 5.01 m^2/g), 0.0069 and 0.0110 mL/g (avg. 0.0083 mL/g), and 4.80 and 9.72 nm (avg. 6.98 nm), respectively. However, sandstones had large PVs, medium SSAs, and average pore diameters. The PVs, SSAs, and average pore diameters varied from 0.0033 to 0.0131 mL/g (avg. 0.0073 mL/g), 0.80 to 4.73 m^2/g (avg. 3.33 m^2/g), and 6.43 to 18.10 nm (avg. 10.71 nm), respectively.

3.3.2 Characterization of PSD

The PSDs of CURs can be classified into two types according to the N_2GA analysis. For coals, Type I showed a unimodal distribution (Fig. 7(a)), whereas Type II had a bimodal distribution with a major peak between 5 nm and 150 nm, as shown in Fig. 7(b). For shales, although Types I (Fig. 7(c)) and II (Fig. 7(d)) were bimodally distributed with a dominant peak of < 3 nm, the minor peaks of Type I and Type II were characterized by sharp and gentle distributions, respectively. For sandstones, Type I showed

Table 1 Representative information of the tested samples

Sample ID	HMIP			N_2GA			CO_2GA			Porosity /%	Permeability mD	R_o /%	TOC /%	XRD				NMR	
	TPV/ ($cm^{-3}·g^{-1}$)	SSA/ ($m^2·g^{-1}$)	d/nm	TPV/ ($cm^{-3}·g^{-1}$)	SSA/ ($m^2·g^{-1}$)	d/nm	TPV/ ($cm^{-3}·g^{-1}$)	SSA/ ($m^2·g^{-1}$)	d/nm					C /%	Q/%	F/%	C/%	T_{2cuoff}/%	EP/%
C1	0.0384	20.15	7.6	0.0011	0.21	20.42	0.0660	208.85	0.501	5.00	0.00203	2.37	84.90	9.8	4.3	0.1	0.6	0.97	0.25
C2	0.0374	19.62	7.6	0.0056	1.36	16.52	0.0840	270.68	0.479	4.71	0.04201	2.90	76.45	23.1	0.3	0.0	0.2	1.15	0.62
C3	0.0375	6.47	23.2	0.0015	0.44	13.87	0.0780	256.20	0.501	5.11	0.06137	2.86	88.65	10.9	0.5	0.0	—	0.97	0.74
C4	0.0326	18.64	7	0.0007	0.09	33.76	0.0680	211.09	0.501	4.20	0.01356	2.46	83.50	9.6	4.6	1.3	0.8	1.12	0.30
C5	0.0343	19.01	7.2	0.0009	0.61	6.76	0.0610	203.76	0.501	4.46	0.00160	2.44	81.34	5.8	6.4	1.7	1.2	2.65	0.16
C6	0.037	20.03	7.4	0.0024	1.01	9.51	0.0710	229.91	0.479	4.77	0.03391	2.55	83.20	10.8	3.1	0.2	0.3	1.32	0.61
C7	0.0388	20.40	7.6	0.0007	0.17	17.21	0.0750	237.99	0.479	4.98	0.02810	2.69	84.29	6.8	7.7	0.4	0.8	0.87	0.31
C8	0.0425	23.35	7.3	0.0007	0.12	23.40	0.0680	209.77	0.501	5.19	0.00108	2.42	90.10	7.2	1.8	0.5	0.4	3.72	0.13
C9	0.0292	7.08	16.5	0.0008	0.35	8.61	0.0560	166.74	0.501	4.02	0.03403	2.15	80.82	5.2	7.2	0.9	0.7	1.52	0.33
S1	0.0054	1.28	16.8	0.0087	4.33	7.99	0.0030	10.06	0.860	0.66	0.00010	2.56	2.67	54.9	37.8	3.0	1.1	3.51	0.09
S2	0.0068	2.55	10.6	0.0110	5.83	7.53	0.0040	13.09	0.865	1.47	0.00010		3.25	53.7	38.0	4.0	—	12.33	0.06
S3	0.0038	1.15	13.2	0.0073	2.97	9.73	0.0017	6.02	0.829	0.86	0.00006		2.13	41.6	39.1	7.4	11.7	37.65	0.02
S4	0.0092	1.43	25.7	0.0084	3.67	9.10	0.0015	4.89	0.840	2.43	0.00018	2.58	1.46	43.4	39.7	7.5	9.4	6.14	0.09
S5	0.0077	0.69	44.4	0.0087	5.00	6.92	0.0028	8.92	0.913	1.92	0.00022		2.50	50.8	47.3	1.9	—	2.31	0.10
S6	0.0035	0.52	24.1	0.0084	6.00	5.59	0.0030	8.41	0.912	0.78	0.00011	2.54	2.89	42.0	45.0	4.0	8.0	10.72	0.09
S7	0.0087	0.28	12.6	0.0076	5.37	5.62	0.0024	8.04	0.848	2.25	0.00230		1.42	41.5	56.9	1.6	—	1.15	0.21
S8	0.0062	0.40	61.8	0.0084	6.98	4.81	0.0037	12.22	0.882	1.59	0.00132		2.89	51.5	36.4	3.6	6.5	3.05	0.13
S9	0.0074	0.07	41.9	0.0069	4.94	5.54	0.0018	6.10	0.849	2.65	0.00164	2.69	1.25	39.7	45.8	2.4	12.1	1.15	0.18
T1	0.0075	0.90	33.5	0.0044	1.15	15.43	0.0005	1.63	0.927	1.98	0.00097		0.78	29.2	45.1	0.0	25.7	1.15	0.47
T2	0.0098	0.72	54.8	0.0057	2.21	10.24	0.0009	2.97	0.831	2.18	0.00085		0.34	14.0	63.0	19.0	4.0	1.00	0.47
T3	0.0066	0.76	34.8	0.0062	2.27	10.90	0.0009	3.09	0.877	1.59	0.00005		—	22.0	44.0	13.0	21.0	3.42	0.11
T4	0.0084	0.80	42	0.0056	1.23	18.10	0.0009	3.17	0.885	1.19	0.00015		—	16.0	51.0	20.0	13.0	1.00	0.23
T5	0.0188	0.94	80.5	0.0033	0.81	16.15	0.0002	0.93	0.793	4.11	0.00425		—	8.0	78.0	14.0	—	1.00	0.38
T6	0.0114	1.84	24.7	0.0092	4.53	8.07	0.0019	6.26	0.906	2.50	0.00064		0.07	46.0	53.0	1.0	—	2.31	0.42
T7	0.0134	0.99	54.3	0.0051	2.50	8.10	0.0004	1.55	0.811	3.47	0.00378		0.23	22.0	70.6	3.9	3.5	2.31	0.57
T8	0.0117	1.87	25.1	0.0100	4.73	8.42	0.0023	7.61	0.867	3.05	0.00207		2.34	48.3	39.9	2.8	9.0	1.15	0.63
T9	0.0116	1.31	35.3	0.0131	6.40	8.19	0.0032	10.40	0.869	3.32	0.00015		2.24	29.7	37.6	2.6	30.1	10.72	0.21
T10	0.0119	2.09	22.7	0.0129	8.01	6.43	0.0029	9.14	0.918	3.08	0.00011		3.26	45.0	39.6	3.4	10.6	1.15	0.12
T11	0.0114	1.24	36.8	0.0053	2.75	7.72	0.0036	11.43	0.898	2.86	0.00051		4.56	25.6	52.4	0.8	0.0	12.33	1.75

Notes: C: clay; Q: quartz; F: feldspar; C: carbonate; EP: effective porosity.

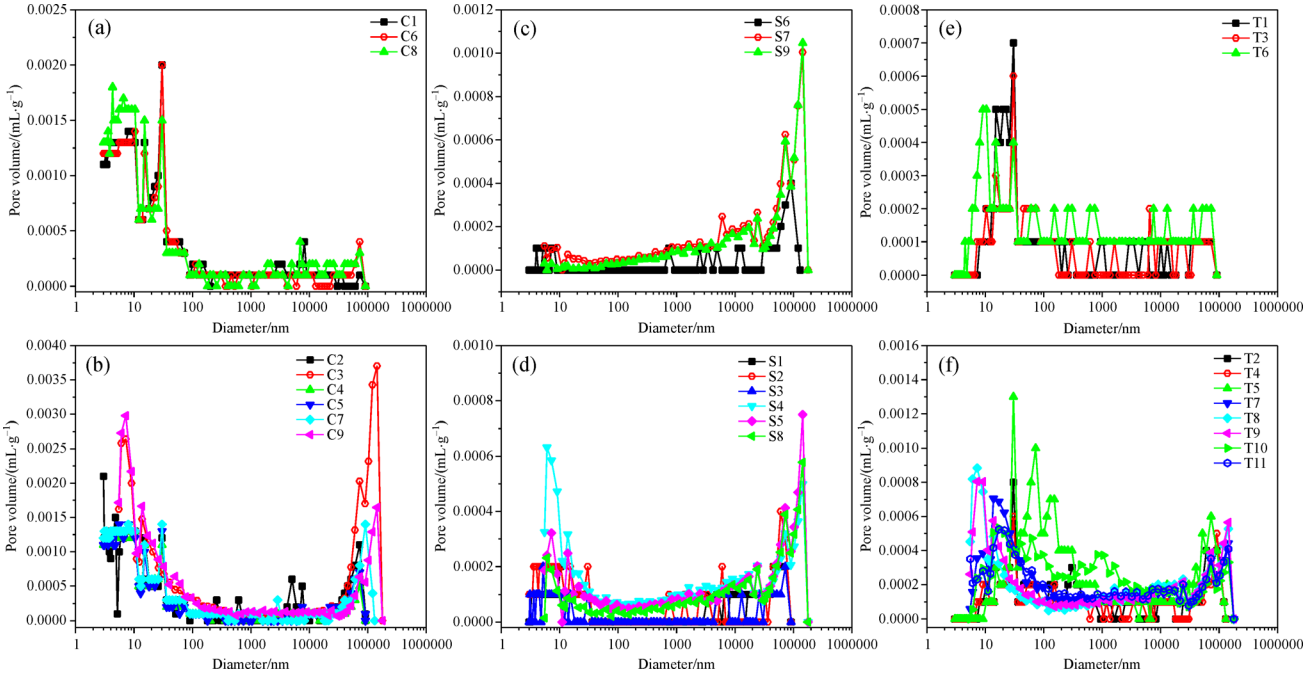

Fig. 5 PSDs of CURs obtained from HMIP analysis: (a) and (b) coals; (c) and (d) shales; (e) and (f) sandstones.

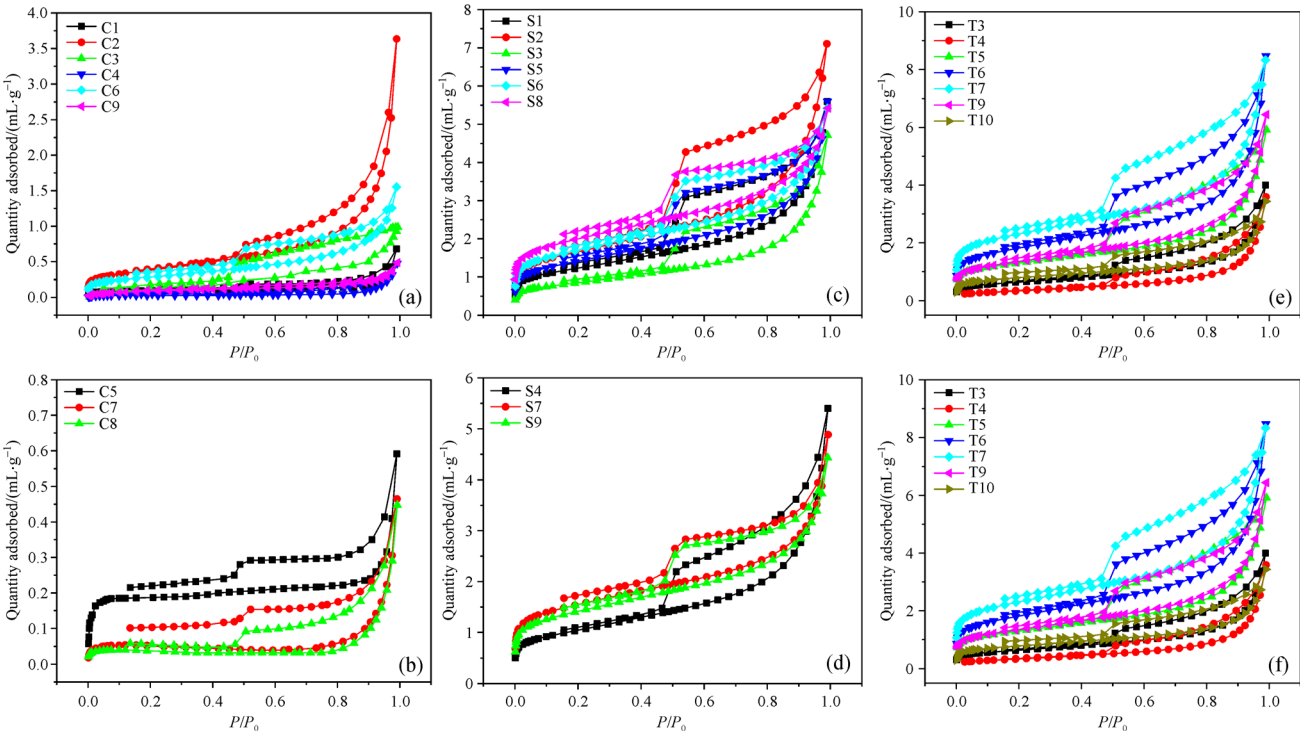

Fig. 6 Hysteresis loop types and the corresponding pore shapes in CURs: (a) and (b) coals; (c) and (d) shales; (e) and (f) sandstones.

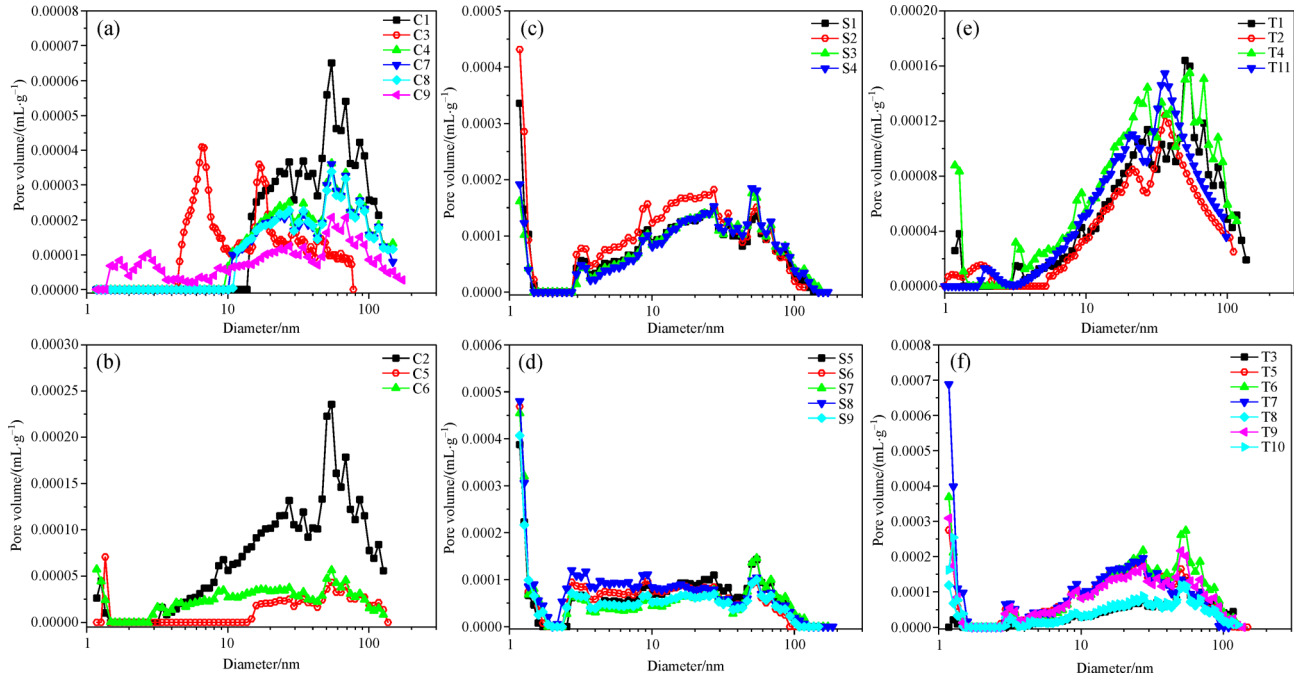

Fig. 7 PSDs of various reservoirs according to N_2GA: (a) and (b) coals; (c) and (d) shales; (e) and (f) sandstones.

a high pore volume of pores of 5–100 nm (Fig. 7(e)), and Type II showed a bimodal distribution, with modes at around < 3 nm and 5–100 nm, as shown in Fig. 7(f).

3.4 CO_2GA analyses

3.4.1 Physical properties and pore types

The CO_2GA adsorption isotherms of CURs were manifested as Type I curves recommended by the IUPAC, as shown in Fig. 8, indicating that micropores were well-developed. DFT PV, SSA, and average pore diameter of CURs samples are shown in Table 1. From the results of CO_2GA measurements, coals were characterized by high PVs (0.122–0.171 mL/g) and SSAs (166.74–270.68 m^2/g), and small average pore diameters (0.48–0.50 nm). Shales were characterized by medium PVs, SSAs, and average pore diameters. Their TPVs, SSAs, and average pore diameters, ranging from 0.0015 to 0.004 mL/g, 4.89 to 12.22 m^2/g, and 0.83 to 0.91 nm, respectively. However, sandstones had poor PVs and SSAs, but large pore diameters. The TPVs, SSAs, and average pore diameters were between 0.0002 and 0.0036 mL/g, 0.93 and 11.43 m^2/g, and 0.81 and 0.93 nm, respectively.

3.4.2 Characterization of PSDs

Figure 9 shows the PSDs of the micropores of CURs determined by CO_2GA results. For coals, the plot of the derivation of PV with variation in pore diameter had two major peaks at around 0.4–0.5 and 0.5–0.7 nm, and a minor peak between 0.7 and 1.0 nm, as shown in Fig. 9(a). The PSDs of shales and sandstones showed multimodal distribution (Figs. 9(b) and 9(c)) with two peaks at around

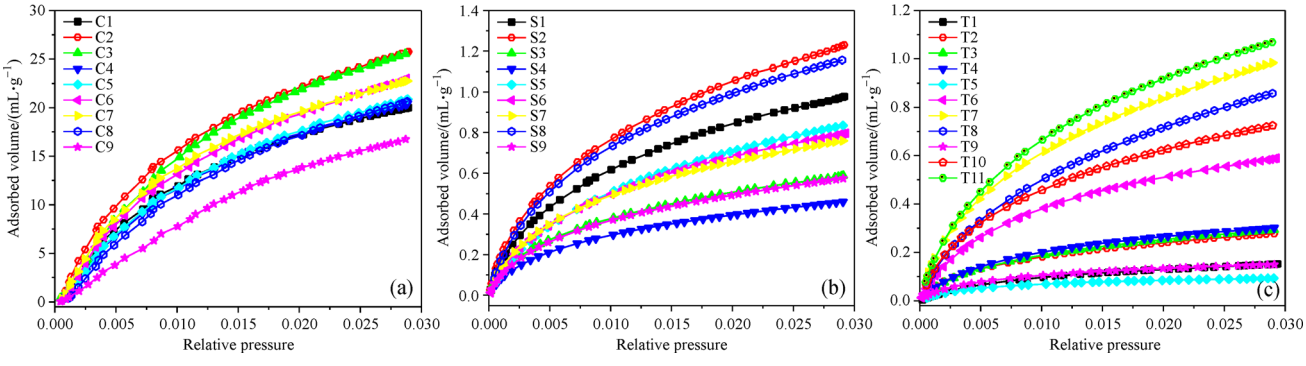

Fig. 8 CO_2GA adsorption isotherms of (a) coals, (b) shales, (c) sandstones.

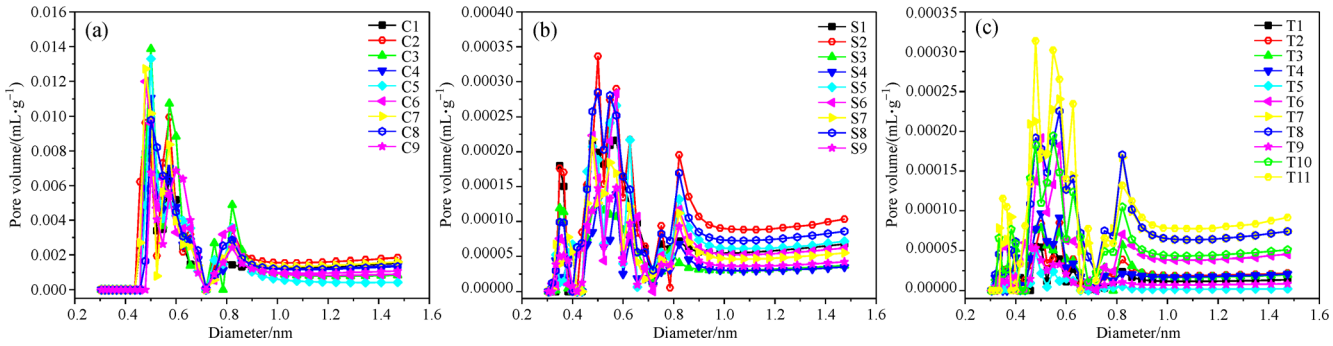

Fig. 9 PSDs of CURs described by CO_2GA: (a) coals, (b) shales, (c) sandstones.

0.4–0.5 and 0.5–0.7 nm, as well as two minor peaks at approximately 0.3–0.4 and 0.8–1.0 nm, respectively.

3.5 NMR analyses

The results of NMR T_2 spectrums of CURs were shown in Fig. 10. T_2 distributions of incremental porosity and cumulative porosity can be described by NMR analysis (Lai et al., 2018; Hou et al., 2019), and relevant parameters, such as NMR porosity, $T_{2cutoff}$ values, and effective porosity, can be calculated from the NMR data (Yao and Liu, 2012; Daigle et al., 2014). Different reservoirs had diverse distributions in terms of the T_2 spectrums. The T_2 spectrums of sandstone samples showed a continuous unimodal distribution with a wide peak at around 0.02–1000 ms (Fig. 10(c)), indicating that different scale pores were developed with high pore connectivity. For shales, the T_2 spectrums had a bimodal distribution with two continuous peaks between 0.02 and 1 ms and 3.0–30 ms, respectively (Fig. 10(b)), indicating that micropores and mesopores were well developed with suitable pore connectivity. However, the T_2 spectrums of coals displayed a bimodal distribution with a significant difference between the major and minor peak areas, as shown in Fig. 10(a). Moreover, the main peak (0.04–2.0 ms) and minor peak (20–100 ms) were separated and distinct from each other, indicating micropores dominant pore systems with poor pore connectivity (Liu et al., 2017).

Previous studies proposed that when the cumulative porosity for the centrifuged status reaches its maximum values, a horizontal projection line can be obtained from the centrifuged cumulative curve to the saturated cumulative curve, providing the $T_{2cutoff}$ value, as shown in Fig. 10 (Gao and Li, 2016; Lai et al., 2018). For instance, the $T_{2cutoff}$ of all the coal, shale, and sandstone samples ranged from 0.87 to 2.65 ms (avg. 1.59 ms), 1.15–37.65 ms (avg. 8.67 ms), and 1.00–12.33 ms (avg. 3.41 ms), respectively. The $T_{2cutoff}$ separated the total pore volume into effective pores and closed pores (Gao and Li, 2016). Gas flow paths connected by pores of relatively large sizes ($T_2 > T_{2cutoff}$) were expected to be effective pores in the NMR analysis (Lai et al., 2018). Further, the proportions of effective porosity in CURs can be then obtained according to the distributions of $T_{2cutoff}$ values and that of coals, shales, and sandstones ranged from 0.73% to 13.48% (avg. 6.71%), 1.90% to 13.84% (avg. 7.03%), and 4.45% to 55.54% (avg. 18.79%), respectively.

4 Discussions

4.1 Full PSDs and microcosmic pore parameters

Previous studies suggested that the pore structure of micropores (<2 nm), mesopores (2–50 nm), and macropores (>50 nm) determined by CO_2GA, N_2GA, and HPMI, respectively, are reliable (Wang et al., 2014). Further, the full PSDs of CURs can be obtained by

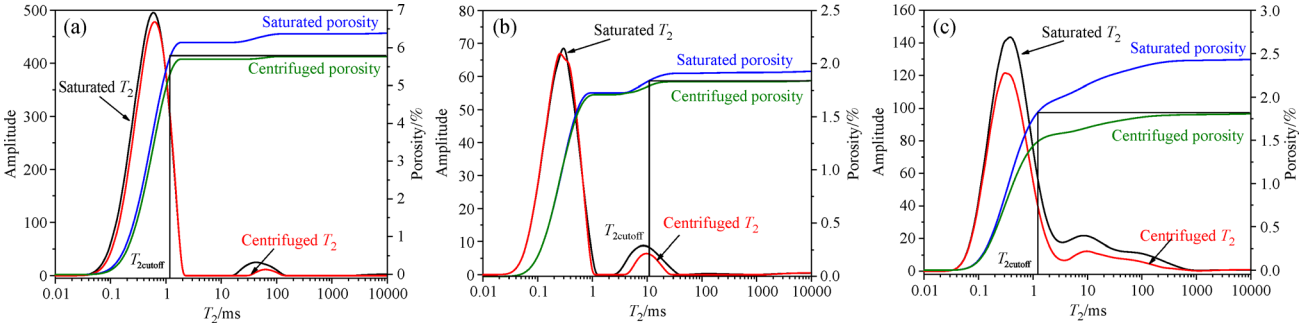

Fig. 10 NMR T_2 spectra including the incremental T_2 distributions and $T_{2cutoff}$ values for (a) coals, (b) shales, (c) sandstones.

combining the results of CO_2GA, N_2GA, and HPMI. Results show that although all the samples exhibited multimodal PSDs, PSDs of different reservoirs had distinct characteristics, as shown in Fig. 11. Generally, the porosities and PVs of CURs were ranked as follows: coal > sandstone > shale; whereas the SSAs were in the order of coal > shale > sandstone, as shown in Fig. 12.

In coals, micropores were the dominant type and account for the majority of PV and SSA, followed by mesopores, whereas macropore was poorly developed (Fig. 11(a) and Fig. 12). The micropore PVs of coals were between 0.0557 and 0.0840 mL/g (avg. 0.0696 mL/g), accounting for 82.61%–92.96% of TPV. The micropore SSAs varied from 166.74 to 270.68 m^2/g (avg. 221.66 m^2/g), contributing to more than 99.49% of the total SSA (Fig. 12). For shales, mesopores and macropores provided the main PV, ranging from 0.0033 to 0.0055 mL/g (avg. 0.0041 mL/g), and 0.0020–0.0081 mL/g (avg. 0.0048 mL/g), respectively. The micropore SSAs range from 6.10 to 13.09 m^2/g (avg. 8.96 m^2/g), accounting for 67.10%–84.59% (avg. 76.78%) of the total SSAs. Different from coals and shales, pores in sandstones were mainly dominated by macropores. The macropore PVs varied from 0.0020 to 0.0081 mL/g (avg. 0.0048 mL/g) which account for 44.42%–89.22% (avg. 57.69%) of the TPV. Mesopore PVs were between 0.0015 and 0.0056 mL/g (avg. 0.0033 mL/g). Micropores were poorly developed in sandstones, but they account for the majority of SSA (31.68%–74.57%).

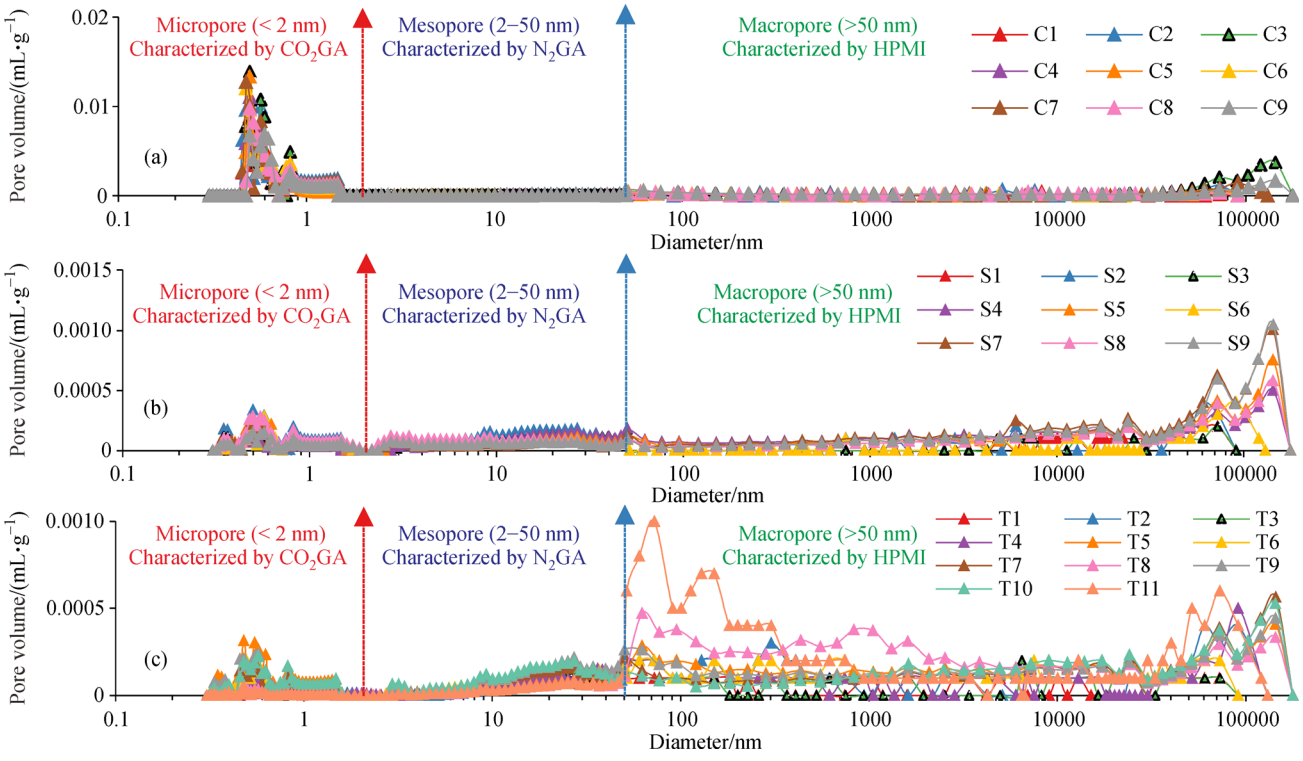

Fig. 11 Full scale PSDs of CURs: (a) coals; (b) shales; (c) sandstones.

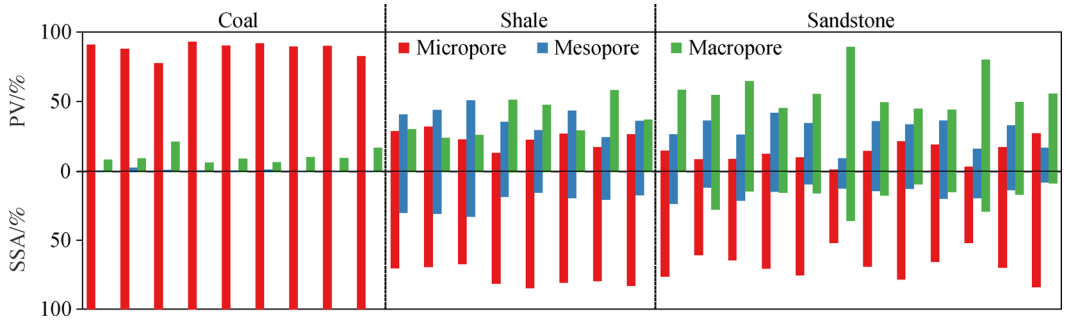

Fig. 12 Microcosmic pore parameters of CURs.

4.2 Relationship between organic-inorganic components and pore structure

Significant differences were observed in the organic-inorganic components of the CURs. Moreover, the results of optical microscopy and FE-SEM had marked differences in pore types and pore development among different organic-inorganic components. Therefore, correlation analyses were performed between different organic-inorganic components and pore structure parameters of the samples, as shown in Fig. 13. There was a weak relationship between TOC and PV in coals, as shown in Fig. 13(a), because coal pores were dominated by micropores, which mainly developed in organic macerals. Coals as a typical aggregated organic matter provide a sufficient material base for micropore development and thus pore development is mainly controlled by coalification level. The source rocks of the study area were predominantly in the overmature stage, and all oxygen functional groups in coal molecules had been basically shed, resulting in weak effects of compaction and dehydration on pore development (Song et al., 2017). Under a temperature-controlled environment, the aromatization degree of coal molecular structure increased significantly with the directional arrangement of aromatic layers, forming a large number of blowholes (Liu et al., 2017). In addition, organic macerals are easily compressed by stress acting in coals, resulting in significant decreases in mesopore and macropore development during the rapid subsidence stage (Xiong et al., 2017). In contrast, clay content had a strong association with macropore PV (R^2 = 0.92; Fig. 13(b)) and macropore SSA (R^2 = 0.55; Fig. 13(e)), indicating that mesopores were mainly developed in clay minerals. FE-SEM observations of intraparticle pores in clay aggregates and interparticle pores between clay mineral layers were helpful in verifying this conclusion.

For shales, micropore PV and micropore SSA were positively associated with TOC (R^2 = 0.68; Figs. 13(g) and 13(j)), indicating that the micropores were mainly organic micropores. The clay content showed a significant positive correlation with mesopore PV and mesopore SSA, as shown in Figs. 13(h) and 13(k), suggesting macropores were mainly developed in clay minerals. In contrast, quartz content had a weak correlation with macropore PV (R^2 = 0.39; Fig. 13(i)) because rigid quartz grains, as a part of the pore framework of shales, can preserve primary intergranular pores developed during burial. Microfractures also occurred along the edge of rigid quartz grains.

For sandstones, a positive correlation was found between TOC and micropore PV (R^2 = 0.77; Fig. 13(m)), which suggests that organic matter was an important contributor to micropores. Moreover, clay content had a strong correlation with mesopore PV and mesopore SSA (Figs. 13(n) and 13(q)), which suggested that clay mineral was the main contributor to mesopores. In terms of the positive relationship between quartz content and macropore PV (R^2 = 0.57; Fig. 13(o)), we suggested that intergranular pores and microfractures can be preserved well to a high degree in sandstones with abundant rigid quartz grains because they did not undergo significant compaction during deep burial stages (Lai et al., 2018).

4.3 Controls of pore structure on petrophysical properties

4.3.1 Effect of pore structure on adsorption capacity

The effects of mesopores and macropores on the adsorption capabilities of CURs can be described through the N_2GA analysis. The N_2GA analysis can be applied to determine the pore structure and N_2 adsorption capability of mesopores and some macropores (50–150 nm). Similarly, the relationship between micropore and adsorption capability can be determined using CO_2GA results (Song et al., 2017). There was a positive correlation between the N_2 adsorption capabilities and mesopore SSAs of various CURs ($R^2 > 0.52$) and a weak relationship between N_2 adsorption capabilities and mesopore SSAs, as shown in Figs. 14(a), 14(c) and 14(f) (Hou et al., 2020c). CO_2 adsorption capabilities had a significantly positive relationship with micropore SSAs (Figs. 14(b), 14(d), 14(e); $R^2 > 0.97$), which suggested that the adsorption capabilities are mainly controlled by micropores because micropore SSAs dominant the total SSAs of CURs. As stated above, clay minerals were an important contributor to mesopores, and minor clay minerals in coals resulted in poor mesopores and low N_2 adsorption capability in coals compared with shales and sandstones as shown in Figs. 14(a), 14(c), and 14(f). However, the CO_2 adsorption capability of coals was far greater than that of shales and sandstones (magnitudes difference) because coals contained abundant organic matters with massive micropores, which provided sufficient SSAs for gas sorption.

4.3.2 Controlling mechanism of pore structure on permeability

As stated above, there was no clear relationship between total porosity and permeability. However, NMR measurements showed a significantly positive correlation between coal permeability and effective porosity, as shown in Fig. 15. Moreover, macropore PV was strongly correlated to permeability (R^2 = 0.58), and the relationship gradually weakened with micropores and mesopores (Fig. 15(a)), suggesting that the pore connectivity of coal decreased with a decrease of effective pores. Macropores and microfractures connected by effective micropores and mesopores promoted the gas seepage through CURs. For sandstones and shales, strong relationships also existed between effective porosity and permeability, as shown in Figs. 15(b) and 15(c). Sandstones and shales had high pore

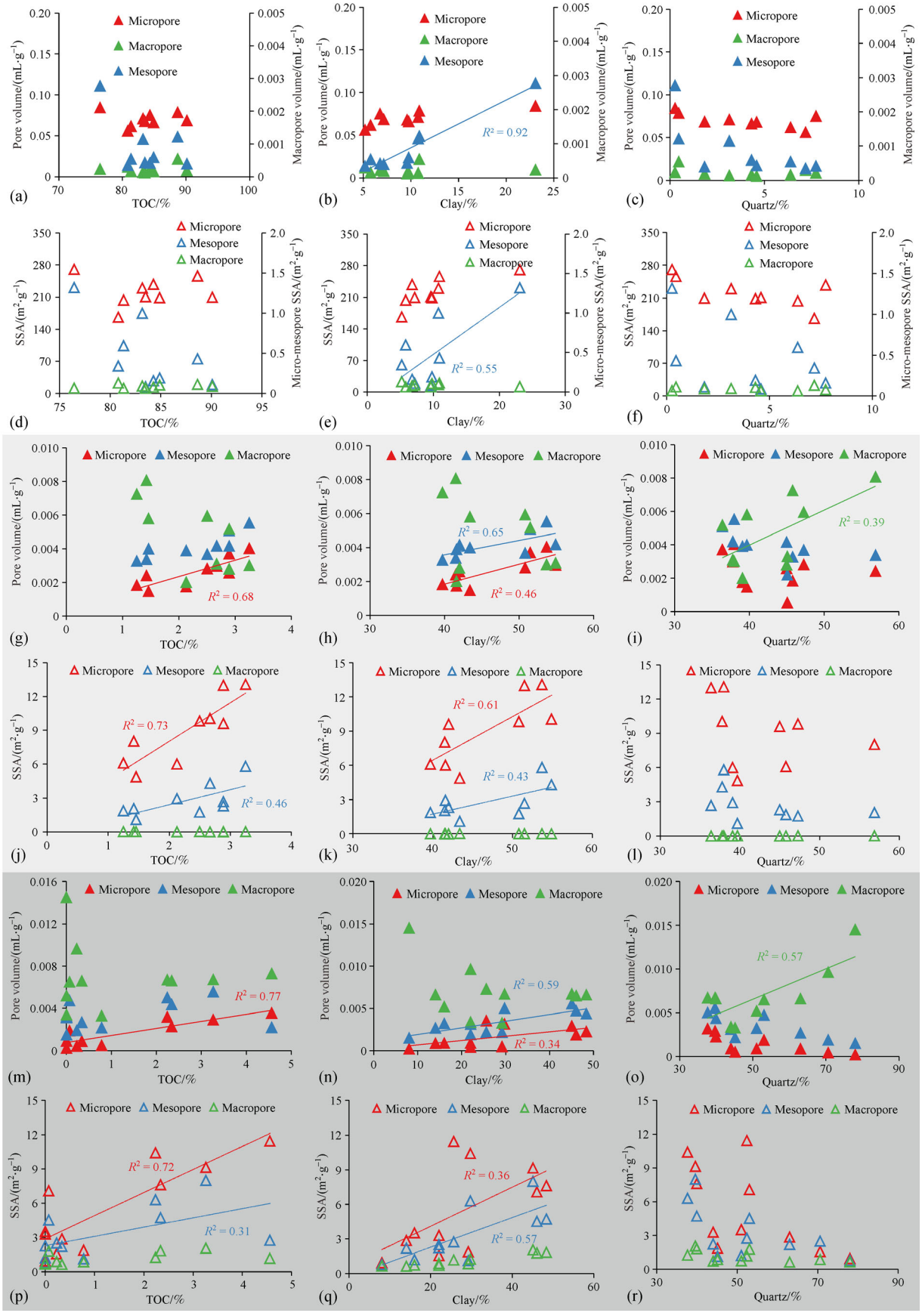

Fig. 13 Relationships between organic-inorganic components and pore structure of CURs: (a)–(f) coals; (g)–(l) shales; (m)–(r) sandstones.

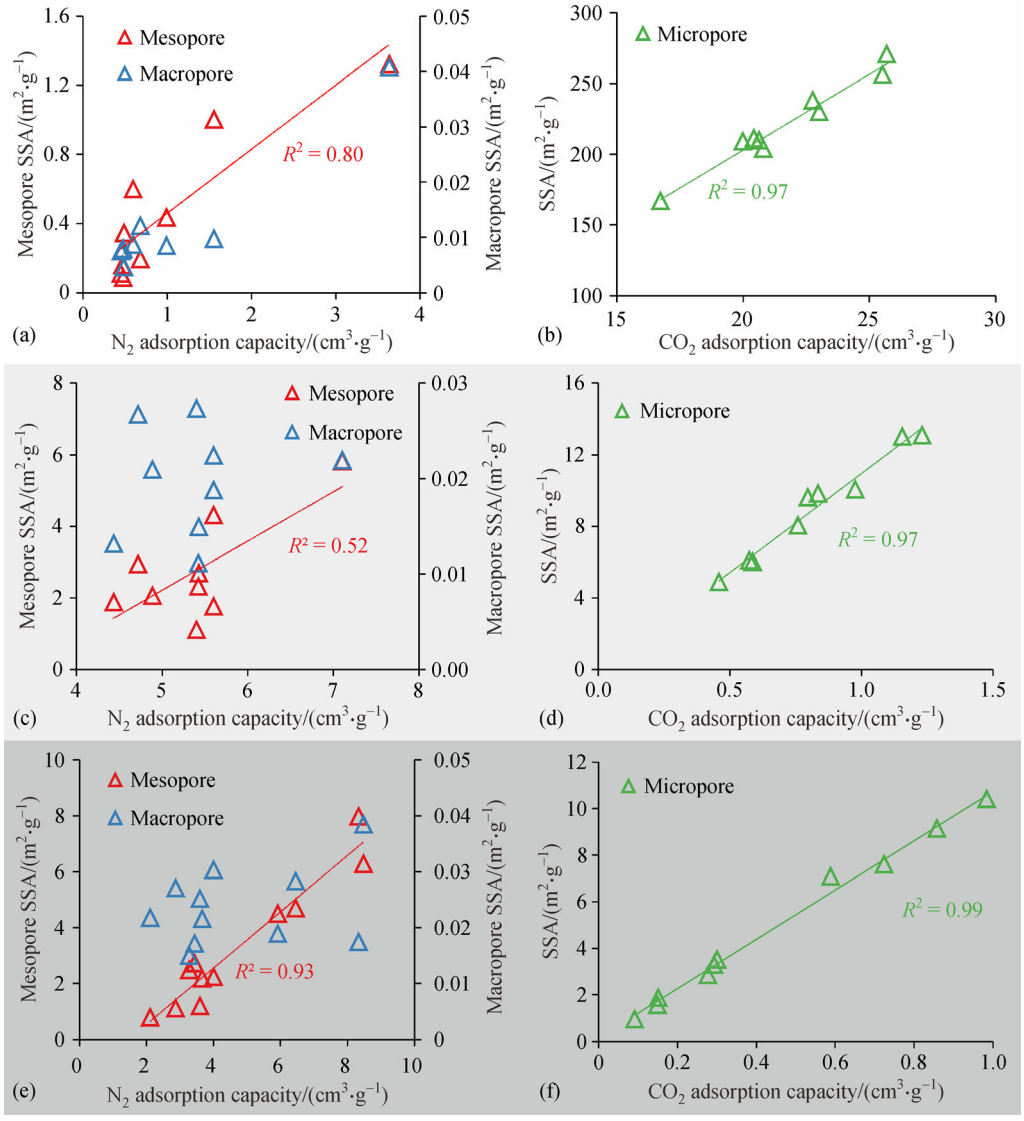

Fig. 14 Effect of pore structure on the adsorption capacity of CURs: (a) and (b) coals; (c) and (d) shales; (e) and (f) sandstones.

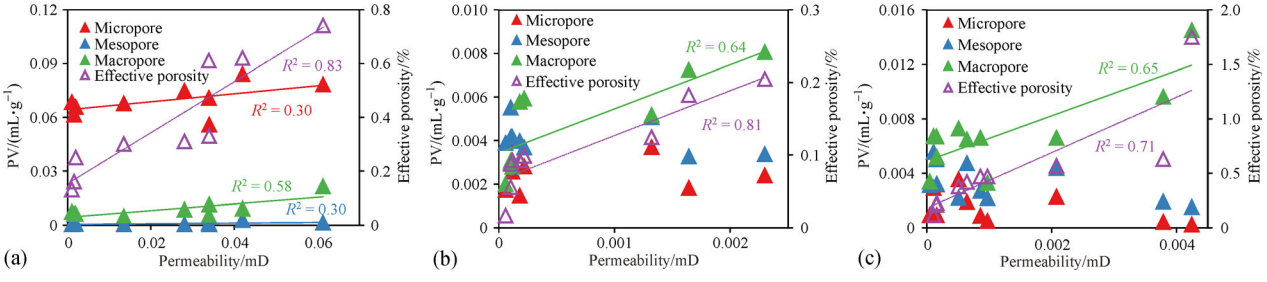

Fig. 15 Relationship between pore structure and permeability of (a) coals, (b) shales, (c) sandstones.

connectivity and a large proportion of effective pores, which enhanced the interconnectivity of macropores and microfractures (Schmitt et al., 2015). Therefore, the effective pores were the main contributor to the permeability of CURs.

5 Conclusions

This study conducts a series of experimental measurements for determining the complex pore structure of CURs, theoretical analysis on the effect of pore structure on the

petrophysical properties. Based on the findings of the study, the conclusions are obtained as follows:

1) Coals have the largest porosity, permeability, and adsorption capability among different CURs. The pore system mainly consists of abundant organic pores and microfractures within macerals. The strong adsorption capability is expected to be in coals because of the predominance of micropores, which provide large SSA for gas adsorption. However, pore connectivity is poor due to the minor proportion of the effective porosity, which strongly determines gas transport behaviors in coals.

2) Shales are characterized by the lowest porosity and permeability. Mesopores and macropores are well developed and account for the main PV. Micropores are also observed in organic matters, accounting for the majority of SSA. The effective porosity of shales accounts for 1.90% to 13.84% of total porosity and positively correlates with permeability.

3) Sandstones have high porosity and permeability. The PV of sandstones is mainly provided by mesopores and macropores. Micropores are poorly developed in sandstones, whereas that attributes to the majority of SSA, resulting in weak gas adsorption capacity. Moreover, the permeability of sandstones is also highly related to the development of effective porosity, which determines the pore connectivity and in a range of 4.45% to 55.54%.

The conclusions in this study are expected to promote the understanding of the complex pore structure of CURs and the effects of different components on the development of multiscale pores. Furthermore, more efforts should be focused on the controlling mechanisms of multiscale pore systems on gas flow behavior within a continuous gas system for long-term co-production of CUNG.

Acknowledgements The authors would like to acknowledge the financial support of the National Natural Science Foundation of China (Grant Nos. 42102208, 41802183 and 41872132) and the Fundamental Research Funds for the Central Universities (JZ2021HGQA0265). The authors declare no competing financial interest.

References

Ayers W B (2002). Coalbed gas systems, resources, and production and a review of contrasting cases from the San Juan and Powder River basins. AAPG Bull, 86: 1853–1890

Bernard S, Horsfield B, Schulz H, Wirth R, Schreiber A, Sherwood N (2012). Geochemical evolution of organic-rich shales with increasing maturity: a STXM and TEM study of the Posidonia Shale (Lower Toarcian, northern Germany). Mar Pet Geol, 31(1): 70–89

Chen S, Zhu Y, Li W, Wang H (2012). Influence of magma intrusion on gas outburst in a low rank coal mine. Int J Min Sci Technol, 22(2): 259–266

Daigle H, Thomas B, Rowe H, Nieto M (2014). Nuclear magnetic resonance characterization of shallow marine sediments from the Nankai Trough, Integrated Ocean Drilling Program Expedition 333. J Geophys Res Solid Earth, 119(4): 2631–2650

Gao H, Li H A (2016). Pore structure characterization, permeability evaluation and enhanced gas recovery techniques of tight gas sandstones. J Nat Gas Sci Eng, 28: 536–547

Ghomeshi S, Kryuchkov S, Kantzas A (2018). An investigation into the effects of pore connectivity on T_2 NMR relaxation. J Magn Reson, 289: 79–91

Hou X, Liu S, Zhu Y, Yang Y (2020a). Evaluation of gas contents for a multi-seam deep coalbed methane reservoir and their geological controls: *in situ* direct method versus indirect method. Fuel, 265: 116917

Hou X, Liu S, Zhu Y, Yang Y (2020c). Experimental and theoretical investigation on sorption kinetics and hysteresis of nitrogen, methane, and carbon dioxide in coals. Fuel, 268: 117349

Hou X, Zhu Y, Chen S, Wang Y (2017). Gas flow mechanisms under the effects of pore structures and permeability characteristics in source rocks of coal measures in Qinshui Basin, China. Energ Explor Exploit, 35(3): 338–355

Hou X, Zhu Y, Chen S, Wang Y, Liu Y (2020c). Investigation on pore structure and multifractal of tight sandstone reservoirs in coal bearing strata using LF-NMR measurements. J Petrol Sci Eng, 187: 106757

Hou X, Zhu Y, Wang Y, Liu Y (2019). Experimental study of the interplay between pore system and permeability using pore compressibility for high rank coal reservoirs. Fuel, 254: 115712

Hou X, Zhu Y, Yao H (2018). Coupled accumulation characteristics of Carboniferous-Permian coal measure gases in the Northern Ordos Basin, China. Arab J Geosci, 11(7): 156

Huang H, Sun W, Ji W, Zhang R, Du K, Zhang S, Ren D, Wang Y, Chen L, Zhang X (2018). Effects of pore-throat structure on gas permeability in the tight sandstone reservoirs of the Upper Triassic Yanchang formation in the Western Ordos Basin, China. J Petrol Sci Eng, 162: 602–616

Krooss B M, van Bergen F, Gensterblum Y, Siemons N, Pagnier H J M, David P (2002). High-pressure methane and carbon dioxide adsorption on dry and moisture-equilibrated Pennsylvanian coals. Int J Coal Geol, 51(2): 69–92

Lai J, Wang G, Cao J, Xiao C, Wang S, Pang X, Dai Q, He Z, Fan X, Yang L, Qin Z (2018). Investigation of pore structure and petrophysical property in tight sandstones. Mar Pet Geol, 91: 179–189

Law B E, Curtis J B (2002). Introduction to unconventional petroleum systems. AAPG Bull, 86: 1851–1852

Li X, Kang Y, Haghighi M (2018). Investigation of pore size distributions of coals with different structures by nuclear magnetic resonance (NMR) and mercury intrusion porosimetry (MIP). Measurement, 116: 122–128

Li Y, Cheng Z, Tang D, Gan Q, Niu X, Wang K, Shen R (2017). Coal pore size distributions controlled by the coalification process: an experimental study of coals from the Junggar, Ordos and Qinshui basins in China. Fuel, 206: 352–363

Li Y, Song D, Liu S, Pan J (2020). Characterization of ultramicropores and analysis of their evolution in tectonically deformed coals by low-pressure CO_2 adsorption, XRD, and HRTEM techniques. Energy Fuels, 34(8): 9436–9449

Li Y, Tang D, Wu P, Niu X, Wang K, Qiao P, Wang Z (2016). Continuous unconventional natural gas accumulations of Carboni-

ferous-Permian coal-bearing strata in the Linxing area, northeastern Ordos basin, China. J Nat Gas Sci Eng, 36: 314–327

Li Y, Wang Z, Pan Z, Niu X, Yu Y, Meng S (2019b). Pore structure and its fractal dimensions of transitional shale: a cross section from east margin of the Ordos Basin, China. Fuel, 241: 417–431

Li Y, Yang J, Pan Z, Meng S, Wang K, Niu X (2019a). Unconventional natural gas accumulations in stacked deposits: a discussion of upper paleozoic coal-bearing strata in the east margin of the Ordos basin, China. Acta Geol Sin-Engl, 93(1): 111–129

Liu Y, Zhu Y, Li W, Zhang C, Wang Y (2017). Ultra micropores in macromolecular structure of subbituminous coal vitrinite. Fuel, 210: 298–306

Loucks R G, Reed R M, Ruppel S C, Jarvie D M (2009). Morphology, genesis, and distribution of nanometer-scale pores in siliceous mudstones of the Mississippian Barnett Shale. J Sediment Res, 79 (12): 848–861

Mishra D K, Samad S K, Varma A K, Mendhe V A (2018). Pore geometrical complexity and fractal facets of Permian shales and coals from Auranga Basin, Jharkhand, India. J Nat Gas Sci Eng, 52: 25–43

Monaghan A A (2017). Unconventional energy resources in a crowded subsurface: reducing uncertainty and developing a separation zone concept for resource estimation and deep 3D subsurface planning using legacy mining data. Sci Total Environ, 601-602: 45–56

Nie B, Liu X, Yang L, Meng J, Li X (2015). Pore structure characterization of different rank coals using gas adsorption and scanning electron microscopy. Fuel, 158: 908–917

Ross D J K, Bustin R M (2008). Characterizing the shale gas resource potential of Devonian-Mississippian strata in the Western Canada sedimentary basin: application of an integrated formation evaluation. AAPG Bull, 92(1): 87–125

Rouquerol J, Avnir D, Fairbridge C W, Everett D H, Haynes J M, Pernicone N, Ramsay J D F, Sing K S W, Unger K K, and the IUPAC (International Union of Pure and Applied Chemistry) (1994). Physical chemistry division commission on colloid and surface chemistry, subcommittee on characterization of porous solids: recommendations for the characterization of porous solids (technical report). Pure Appl Chem, 66(8): 1739–1758

Schmitt M, Fernandes C P, Wolf F G, Da Cunha Neto J A, Rahner C P, Santiago Dos Santos V S(2015). Characterization of Brazilian tight gas sandstones relating permeability and Angstrom-to micron-scale pore structures. J Nat Gas Sci Eng, 27: 785–807

Song D, Ji X, Li Y, Zhao H, Song B, He K (2020). Heterogeneous development of micropores in medium-high rank coal and its relationship with adsorption capacity. Int J Coal Geol, 226: 103497

Song Y, Jiang B L J (2017). Nanopore structural characteristics and their impact on methane adsorption and diffusion in low to medium tectonically deformed coals: case study in the Huaibei Coal Field. Energy Fuels, 31(7): 6711–6723

Sun C, Tang S, Zhang S, Wei J, Hou Y, Zhang T (2017). Nanopore characteristics of Late Paleozoic transitional facies coal-bearing shale in Ningwu Basin, China investigated by nuclear magnetic resonance and low-pressure nitrogen adsorption. J Nanosci Nanotechnol, 17(9): 6433–6444

Wang D, Shao L, Li Z, Li M, Lv D, Liu H (2016). Hydrocarbon generation characteristics, reserving performance and preservation conditions of continental coal measure shale gas: a case study of Mid-Jurassic shale gas in the Yan'an Formation, Ordos Basin. J Petrol Sci Eng, 145: 609–628

Wang Y, Zhu Y, Chen S, Li W (2014). Characteristics of the nanoscale pore structure in northwestern Hunan Shale Gas Reservoirs using field emission scanning electron microscopy, high-pressure mercury intrusion, and gas adsorption. Energy Fuels, 28(2): 945–955

Wang Y, Zhu Y, Zhang R, Anovitz L, Bleuel M, Liu S, Chen S (2020). SANS coupled with fluid invasion approaches for characterization of overall nanopore structure and mesopore connectivity of organic-rich marine shales in China. Int J Coal Geol, 217: 103343

Xiao D, Jiang S, Thul D, Lu S, Zhang L, Li B (2018). Impacts of clay on pore structure, storage and percolation of tight sandstones from the Songliao Basin, China: implications for genetic classification of tight sandstone reservoirs. Fuel, 211: 390–404

Xiong F, Jiang Z, Li P, Wang X, Bi H, Li Y, Wang Z, Amooie M A, Soltanian M R, Moortgat J (2017). Pore structure of transitional shales in the Ordos Basin, NW China: effects of composition on gas storage capacity. Fuel, 206: 504–515

Yang Y, Liu S (2020). Laboratory study of cryogenic treatment induced pore-scale structural alterations of Illinois coal and their implications on gas sorption and diffusion behaviors. J Petrol Sci Eng, 194: 107507

Yao Y, Liu D (2012). Comparison of low-field NMR and mercury intrusion porosimetry in characterizing pore size distributions of coals. Fuel, 95: 152–158

Zhang R, Ning Z, Yang F, Zhao H, Wang Q (2016). A laboratory study of the porosity-permeability relationships of shale and sandstone under effective stress. Int J Rock Mech Min, 81: 19–27

Zhao J, Xu H, Tang D, Mathews J P, Li S, Tao S (2016). Coal seam porosity and fracture heterogeneity of macrolithotypes in the Hancheng Block, eastern margin, Ordos Basin, China. Int J Coal Geol, 159: 18–29